AIAA JOURNAL
Vol. 34, No. 4, April 1996

Simulation of Multiple Shock–Shock Interference Patterns on a Cylindrical Leading Edge

Kwen Hsu* and Ijaz H. Parpia†
University of Texas at Arlington, Arlington, Texas 76019-0018

Numerical simulations of hypersonic shock–shock interactions that arise when two shocks impinge on the bow shock in front of a cylinder are presented. Results are shown for both inviscid and laminar viscous flow models, using perfect-gas and equilibrium-air assumptions for a range of incident shock locations. These results are compared with experiment, and with flow patterns identified previously using Edney's method. It has been found that under the conditions simulated here, one suggested interaction flowfield, the pattern of dual type IV supersonic jets, exists only temporarily, eventually transforming to a concomitant-jets pattern. The validity of this numerical result is confirmed by a simulation of the entire transient process in a shock tunnel of the type used in the experimental study.

I. Introduction

SHOCK–SHOCK interaction is one of the key issues associated with the design of hypersonic vehicles. Extreme peak values of aeroheating and pressure loads on the vehicle surface caused by the interaction must be predicted accurately to design an effective vehicle structure.

Interference patterns that are generated by a single shock impinging on the bow shock formed in front of a blunt edge were identified in a pioneering study by Edney.[1] Following Edney's classification of interaction patterns, either a type III or a type IV interaction pattern occurs when the incident shock intersects the bow shock in the subsonic region near the nose of the blunt body. In the type IV case, a supersonic jet is formed inside the shock layer, and this jet may impinge on the body surface. Because of the high heating rate and surface pressure load generated at the point of jet impingement, type IV interaction is of special interest and has been studied the most frequently. Experimental studies of type IV interactions generated by single incident shocks include Refs. 1–4. Numerical studies of these flowfields can be found in, for example, Refs. 5–10.

Holden et al.[11] and Wieting[12] have reported experiments on the type IV interaction in the presence of two incident shocks. More complicated interaction patterns are generated in this case; the peak pressure and heat transfer rate vary in response to changes in the position and strength of the second impinging shock.

The objective of the present study is to simulate the dual shock–shock interaction problem for various flow conditions to acquire a better understanding of this problem. Numerical results are shown for several positions of the second incident shock, and both the perfect-gas model and an equilibrium-air model are used in the simulations. Detailed flow patterns, cylinder surface heat transfer rates, and pressure distributions are compared with experiment.

The structure of two new patterns reported by Wieting,[12] namely, concomitant jets and dual type IV jets, have been investigated. Both of these patterns are closely related to the traditional type IV flowfield, but are more complicated in structure. The difference between the dual-jets pattern and the concomitant-jets pattern is that in the former case, two jets are separated by a subsonic region, while in the latter, the jets are separated merely by a slip line or shear layer.

A quick and effective way to determine the salient features of steady shock–shock interaction patterns is based on the construction of pressure–deflection diagrams. This method was used by Edney[1] in his classification of the six interaction patterns for the case of a single impinging shock, and was also used by Wieting[12] to identify the two new patterns associated with multiple shock impingement. Figure 1 shows the two new patterns together with the relevant pressure–deflection diagrams. Note that the patterns shown in Fig. 1, which are consistent with our numerical simulations and with the discernable flow features reported in Ref. 12, differ in one respect from the pressure–deflection diagrams shown there. Specifically, the expansion between regions 6 and 7 appears to be partially transmitted through the shear layer separating the upper and lower jets. Keep in mind that flow features other than steady shocks and supersonic expansions are ignored in this description, and furthermore, that certain data, such as the shock standoff distance and transmitted shock length, are required if the method is to provide an accurate picture of the interaction flowfield. Thus, the case of two impinging shocks is a rigorous test of the accuracy and usefulness of Edney's method.[1]

In Wieting's work,[12] the dual-jets pattern can be clearly seen in the picture of run 86, while it is surmised that run 85 shows the pattern of concomitant jets. The schlieren photograph taken during run 85 is not very clear, and we show that in this case the experimental results are well complemented by a numerical simulation on a sufficiently dense grid. Other cases in the same series of experiments are also simulated for the purpose of validation, and still more cases (for which no experimental confirmation is available) are included in this study to further understand the physics of shock–shock interaction.

II. Governing Equations

The two-dimensional compressible Navier–Stokes equations, written in conservation form, are

$$\frac{\partial U}{\partial t} + \nabla \cdot (\boldsymbol{F}_I + \boldsymbol{F}_V) = 0 \tag{1}$$

where

$$U = \begin{pmatrix} \rho \\ \rho u \\ \rho v \\ \rho E \end{pmatrix}$$

is the vector of conserved variables, defined in terms of the density ρ; the fluid velocity, which has Cartesian components u, v; and the total energy per unit mass, E, which is the sum of the specific internal energy e and the specific kinetic energy of the fluid,

$$E = e + \tfrac{1}{2}(u^2 + v^2)$$

Received June 2, 1995; revision received Nov. 24, 1995; accepted for publication Dec. 1, 1995.

*Graduate Student, Department of Mechanical and Aerospace Engineering.
†Associate Professor, Department of Mechanical and Aerospace Engineering. Member AIAA.

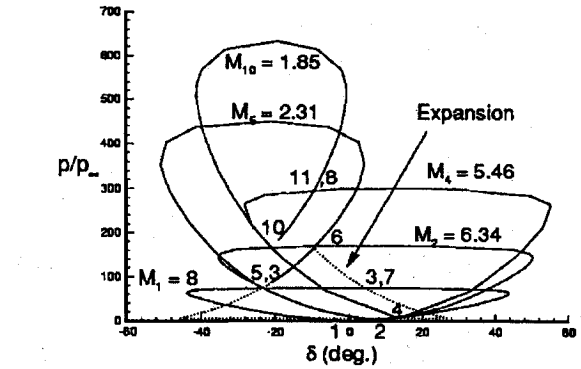

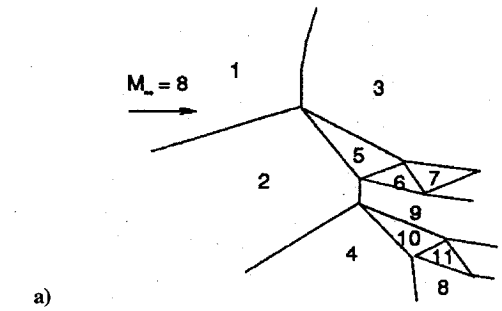

a)

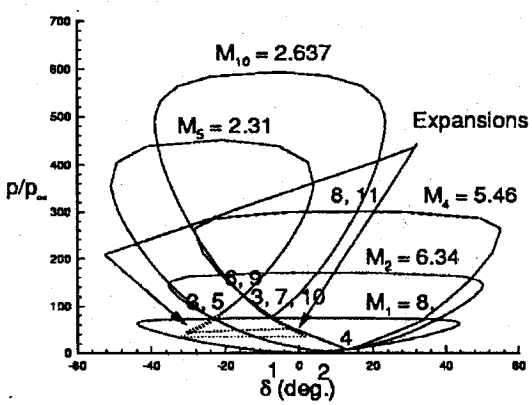

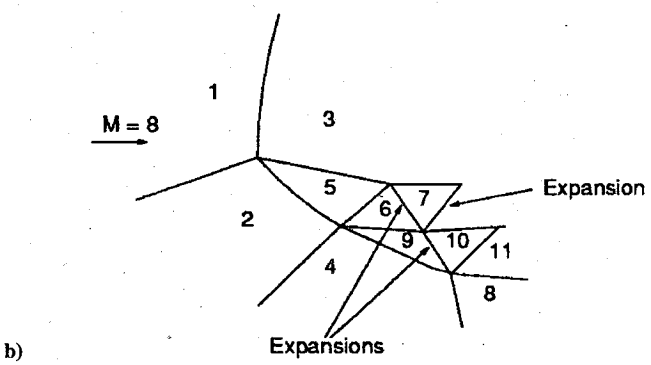

b)

Fig. 1 a) Pressure–deflection diagram for pattern of dual type IV supersonic jets created by incident shocks generated by 7.5- and 5-deg wedges and b) pressure–deflection diagram for concomitant supersonic jets created by incident shocks generated by 7.5- and 5-deg wedges.

The inviscid and viscous parts of the flux are

$$F_I = \begin{pmatrix} \rho u \\ \rho u^2 + p \\ \rho uv \\ \rho uE + up \end{pmatrix} i + \begin{pmatrix} \rho v \\ \rho uv \\ \rho v^2 + p \\ \rho vE + vp \end{pmatrix} j$$

$$F_V = \begin{pmatrix} 0 \\ \sigma_{xx} \\ \sigma_{xy} \\ u\sigma_{xx} + v\sigma_{xy} - q_x \end{pmatrix} i + \begin{pmatrix} 0 \\ \sigma_{xy} \\ \sigma_{yy} \\ u\sigma_{xy} + v\sigma_{yy} - q_y \end{pmatrix} j$$

where p is the pressure, and

$$\sigma_{xx} = -\tfrac{2}{3}\mu[(u_x + v_y) - 3u_x]$$

$$\sigma_{yy} = -\tfrac{2}{3}\mu[(u_x + v_y) - 3v_y]$$

$$\sigma_{xy} = -\mu(u_y + v_x) = \sigma_{yx}$$

The heat flux vector is defined by

$$q = (\mu/Pr)\nabla T$$

where μ is the dynamic viscosity, Pr is the Prandtl number, and T is the temperature. The flow is assumed to be laminar.

The system of equations is completed by the general equation of state

$$p = f(\rho, e)$$

If the Euler equations are chosen to be the flow model, F_V is dropped from the governing equations.

III. Numerical Method

The governing equations are written in finite volume form, which is an application of the integral form of the equations to a cell of area ΔA:

$$\int\int_{\Delta A} \frac{\partial U}{\partial t}\,\mathrm{d}A + \int\int_{\Delta A} \nabla \cdot F\,\mathrm{d}A = 0 \tag{2}$$

where $F = F_I + F_V$. The flux integral is converted to an integral over the cell boundary using Gauss' divergence theorem, and the first term is interpreted as the rate of change of the averaged properties over the cell:

$$\frac{\partial U}{\partial t}\Delta A + \oint_S F \cdot \mathrm{d}s = 0 \tag{3}$$

A structured mesh of quadrilateral cells is chosen for reasons of computational efficiency. In outline, the code incorporates the following features.

The numerical flux through each cell face is evaluated using a second-order MUSCL-type TVD scheme[13] based on Roe's approximate Riemann solver[14] with an entropy correction.[15] Van Albada's flux limiter[16] is used. The modifications developed by Vinokur and Liu[17] for a high-temperature equilibrium gas have also been incorporated into the code.

Either a first- or a second-order time discretization option, depending on the choice of ζ, is available in the discrete implementation of Eq. (3):

$$\frac{\Delta A}{\Delta t}(U^{n+1} - U^n) = (1-\zeta)\sum_{k=1}^{4}[F \cdot \Delta s]_k^{n+1} + \zeta\sum_{k=1}^{4}[F \cdot \Delta s]_k^n$$

When $\zeta = 0.5$, a second-order trapezoidal difference equation in time results, and if $\zeta = 0$, the first order Euler implicit method is selected. For time-accurate calculations, global time-stepping is used, and a Newton–Raphson subiteration scheme with approximate factorization[18] is applied to drive the residual of the discretized equations to small values at each step. Typically, only a few subiterations are needed to reduce the residual to low levels, provided that the time step (or, equivalently, the CFL number) is not too large. Typical values used in this study lie in the range 3–10.

A static grid is assumed at the outset, thereby avoiding the possibility of contamination of the flow due to spurious numerical

signals. This is important, because the type IV interaction is often unsteady.

IV. Flow Simulations

A reflected shock-tube facility was used to create the Mach 8 flow in Wieting's experiment.[12] The shock tunnel consists of a high-pressure driver section and a low-pressure driven section, which are separated by diaphragms. The tunnel is started by rupturing a double diaphragm that permits high-pressure helium in the driver section to expand into the driven section. A normal shock is generated and propagates through the low-pressure air inside the driven section. A region of high-pressure, high-temperature air is produced between this normal shock front and the gas interface between the helium and air. When the shock strikes the end of the driven section, it is reflected, leaving a region of almost stagnant air with extremely high pressure and temperature. Another diaphragm is broken at the inlet of a contoured nozzle to allow the stagnated air to expand through this nozzle and reach the desired Mach number in the test section. Impulsive hypersonic test facilities of this type have extremely short test times: A typical value of 10 ms is reported in Holden et al.[11] and Wieting.[12]

The present numerical study consists of two types of simulations. In the first, the calculations are performed on a single domain that covers only a portion of the front face of the cylinder. Domains of this kind have been used in similar computational studies.[6,7,9,10] In the second type of simulation, the whole tunnel, from the nozzle inlet to the aerodynamic model in the test section, is included in the domain of calculation.

Type IV interaction is often unsteady at a certain level, so a leveling-off of the residual can be taken to be an indication that a limit cycle has been reached. Data such as surface pressure and heat transfer rate distributions are collected after the wave pattern is fully developed with small oscillations of waves around their average positions.

Local Simulations

A single stationary grid that wraps around the front face of the cylinder is used in computations in this category. The domain is just large enough to include all the interactions in the nose region of the model with very few grid points wasted in the freestream region. Simulations of this type are used in most of the studies presented in this paper.

Algebraically generated stretched meshes in which points are clustered in the nose region are used to resolve the interaction pattern. For viscous calculations, grid concentration toward the wall surface is added to resolve the boundary layer.

The flow domain of interest is bounded by inflow, outflow, and wall boundaries. For simplicity of boundary-point procedures, the inflow and outflow boundaries are chosen in such a way that the flow is always supersonic (excluding the boundary-layer flow near the surface). No-slip wall boundary conditions and tangential wall boundary conditions are used for viscous and inviscid calculations respectively. An isothermal wall boundary condition, with wall temperature $T_w = 530°\text{R}$, is specified to be able to compare calculated heat transfer data with those from experiment.

The initial conditions are quite arbitrary as long as they are reasonable enough to initiate the development of the flow toward the correct end state. In closely related computational work by Lind,[8] where single-incident-shock-generated type IV interaction is simulated, the initial condition used is the undisturbed blunt-body solution all over the domain except at the inflow boundary, where freestream and postshock values are specified above and below the shock impingement point and are kept unchanged during the calculation. The initial condition used in the present study is similar to that used by Lind. Freestream conditions are specified all over the domain, with specified and fixed inflow boundary values. Clearly, none of initial conditions discussed here closely models the transient flow in a real tunnel. If only the final quasi-steady-state solution and not the transient is of interest, then previous numerical work indicates that all the initial conditions described above are acceptable. If, on the other hand, the time evolution of the flow around the model in a real shock tunnel is of interest, it is clearly not adequate to use the single-block calculation with such arbitrary initial conditions.

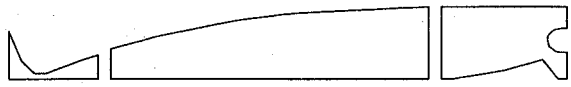

Fig. 2 Zoning of the calculation domain for the successive multiblock calculation (schematic).

Full Shock-Tunnel Simulation

Several major difficulties are encountered in the design of a simulation of this type. Compared to the size of the nozzle throat and the cylinder, the tunnel nozzle exit is very large, so it is not reasonable to use the same number of grid points in both the throat cross section and the nozzle exit cross section. Furthermore, the duration of the simulation is substantially longer than that used in a typical local simulation.

A multiblock gridding technique is adopted to overcome difficulties due to the differing length scales. The tunnel, including the test section and the converging and diverging parts of the nozzle, is divided into three blocks as shown in Fig. 2. The number of grid points across the section of the nozzle doubles at each block interface so that the flow is sufficiently well resolved in the test section. Global conservation at each interface is enforced following the patched-grid method described by Madavan and Rai,[19] and the details of our implementation are given in Ref. 20.

During the long process of flow establishment in the tunnel, not every part of the flow in the tunnel is in variation. A successive-block approach, in which calculations are performed in sequence, is used to reduce the cost of the calculation. In the first stage, just after the tunnel is started, only the first block is active. The second block is activated as the leading shock wave moves downstream into the second block. After all the traveling waves have moved to the downstream portion of the tunnel, the upstream portion of the nozzle becomes stationary, and is taken out of the calculation. It is estimated that this sequential approach cuts down the computation time by about a factor of three.

The grid is clustered toward the nozzle walls using the traditional Poisson grid generation method of Hsu and Lee.[21] Clustering toward the cylinder surface is created by artificial stretching. The grid is also clustered along the impinging shocks (generated by ramps in the test section) and to the cylinder bow shock using the method of Anderson and Munipalli.[22]

A fixed stagnation flow condition is applied at the inlet of the nozzle. To apply this simple inflow boundary condition, the area of the inlet must be considerably larger than that of the throat; otherwise an unphysical total pressure drop will occur. A supersonic outflow boundary condition is imposed on the exit of the test section except on the solid boundary of the cylinder. The initial condition that exists in the experimental facility before the inlet diaphragm is broken is a low-pressure, room-temperature condition. A similar initial condition is used in the present full tunnel calculation.

V. Numerical Results and Discussion

Local Simulation

Simulations for runs 83 and 85–87 in Ref. 12 are presented in this section.

Energy transport by mass diffusion is not important in the cases we simulate here, because the stagnation gas temperature is 2800°R. Consequently, Fourier's law is assumed to be adequate to predict the heat transfer through the wall. It has been found in some previous studies (for example, Refs. 6 and 8, but not 23) that it is difficult to match the numerically predicted heat transfer rate. A grid convergence study for run 87 is shown here because this case was found to be the most computationally challenging. The surface heat transfer shows a very sharp peak that is difficult to reproduce accurately. In addition, the flow is nominally unsteady, and indeed very similar to a traditional type IV interaction flowfield, because the incident shocks begin to coalesce before they interact with the bow shock. The unsteadiness is apparent in the surface pressure and heat transfer distributions, and the plots of the numerical data shown in Figs. 3 and 4 are comparisons of instantaneous values of the predicted surface

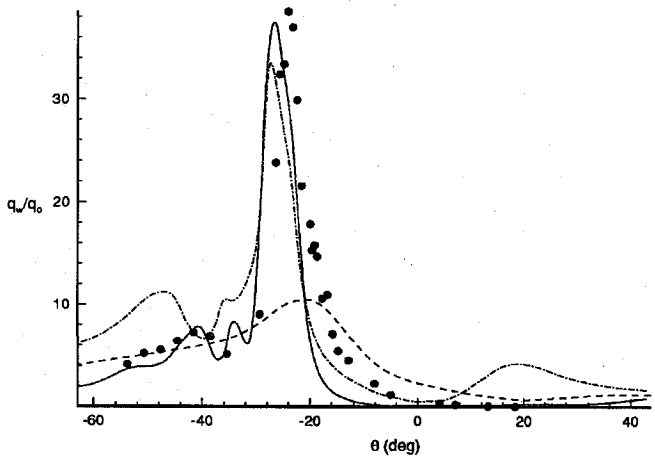

Fig. 3 Surface heat transfer rate, run 87 in Ref. 12; M_∞ = 8.04, δ_1 = 7.5 deg, and δ_2 = 5 deg: ○, experiment; ——, 161 × 181 grid; –·–·–, 161 × 91; and - - - -, 115 × 65.

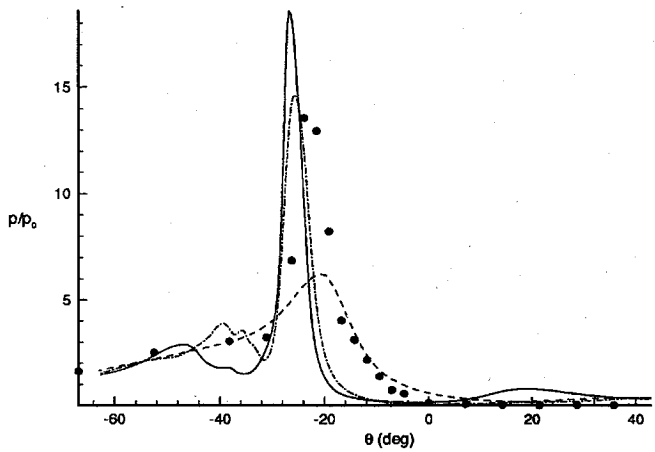

Fig. 4 Surface pressure distribution, run 87 in Ref. 12. M_∞ = 8.04, δ_1 = 7.5 deg, and δ_2 = 5 deg: ○, experiment; ——, 161 × 181; –·–·–, 161 × 91; and - - - -, 115 × 65.

data for the three grids used in a grid-convergence study. Although not shown, many important flow features are lost in the solution on the coarsest grid. There is good qualitative agreement on the finer grids, but as Figs. 3 and 4 show, the grid spacing in the radial direction, which is halved as the 161 × 91 grid is refined to produce the 161 × 181 grid, has a significant effect on the predicted surface loads. The remaining results in this section were generated on the 161 × 91 grid (which has a normal spacing of 1.5×10^{-5} at the wall). In most cases, convergence studies indicate acceptable accuracy on this grid, with the largest disagreement apparent for run 87, which is discussed earlier.

The location of the point on the inflow boundary that separates the freestream from the postshock conditions is determined by knowing the incident shock angles and the positions of the wedges that generate these incident shocks. This information is tabulated in Ref. 12. In the set of computations shown in this section, the point of origin of the first incident shock is held fixed, varying only the point of origin of the second incident shock. The shock strengths are also held fixed.

Interference patterns for runs 85 and 87 are shown in Figs. 5 and 6. As expected, the interference pattern for run 87 is little different from that generated by a single incident shock. In run 85, the incident shocks are clearly separated, and with this level of separation, the concomitant-jets pattern is clearly captured in Fig. 6. Its structure is identical to that predicted using Edney's approximate method.

The pressure distribution along the surface of the cylinder in a Euler solution is shown in Fig. 7. These results using an inviscid gas model are in good agreement with experiment. Small wiggles near the peak appear to be due to insufficient dissipation in the nose region where the jet flow is split into upward and downward streams. The

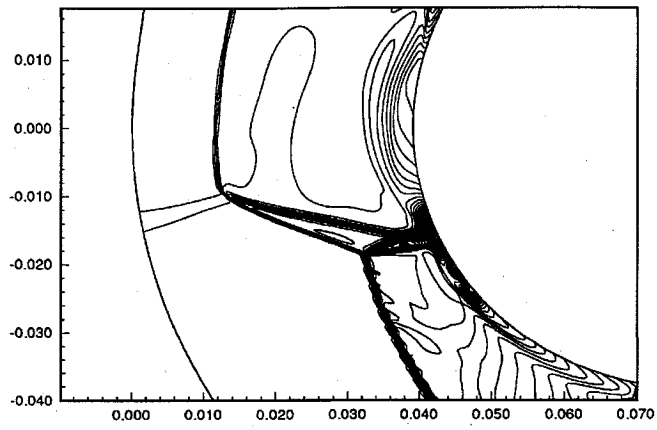

Fig. 5 Computed density contours, run 87 in Ref. 12; M_∞ = 8.04, δ_1 = 7.5 deg, and δ_2 = 5 deg.

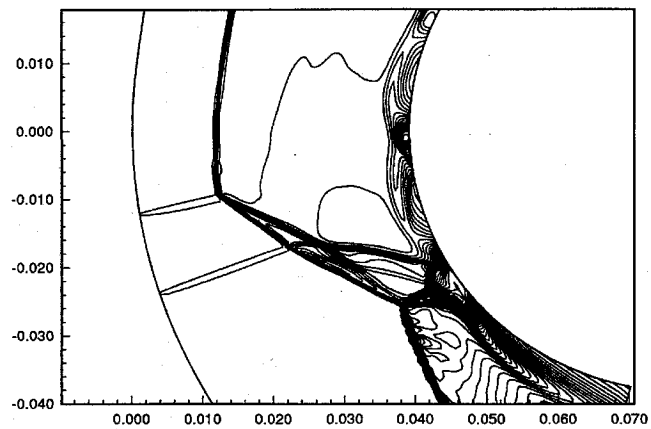

Fig. 6 Computed density contours, run 85 in Ref. 12; M_∞ = 8.04, δ_1 = 7.5 deg, and δ_2 = 5 deg.

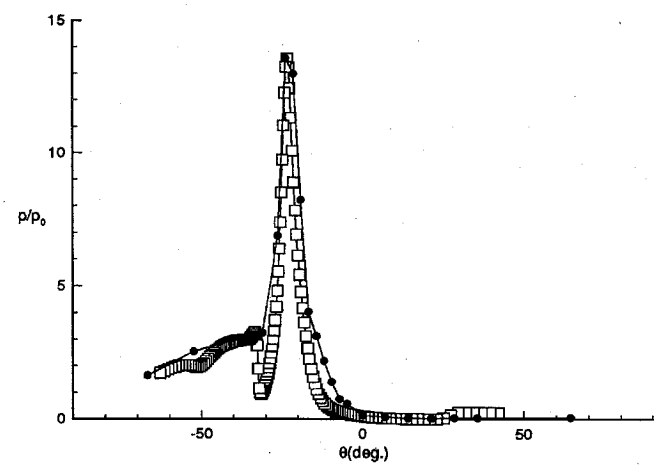

Fig. 7 Computed surface pressure distribution, inviscid flow model, run 87 in Ref. 12: ●, experimental and □, calculated (equilibrium gas).

problem is greatly alleviated in viscous simulations (e.g., Fig. 8). Although not shown here, both the experimental data and computed results for run 85 indicate that the peak surface pressure and heat transfer rate decrease with increasing separation between the incident shocks.

The computed wall pressure distributions for a laminar viscous simulation corresponding to run 83 are presented in Fig. 8 for two different instants. For this case, the numerical solution at an earlier time agrees better with experimental data than the solution at a later time. This may be the result of both experimental and computational errors, or a slight mismatch between the actual test conditions and those used in the simulations.

The flow conditions that result in the pattern of dual type IV jets found in run 86 were simulated assuming inviscid flow and the perfect-gas equation of state. The time evolution of the solution is shown in Fig. 9. As these density contour plots show, the dual-jets pattern may not be an admissible steady-state solution. The dual jets exist only temporarily while the bow shock moves to its final position. Moreover, while the dual-jets pattern exists, the lower jet may in fact be a shear layer instead of a distinct jet. The details of the structure of the lower jet would have to be studied on a much denser grid.

To better understand the transformation of the flow pattern, another time-accurate simulation was performed with both incident shock locations moved up slightly. An equilibrium chemically reacting air model was used. The purpose of making these two changes was to see whether the pattern transition is the result of the difference between the experimental conditions and computational conditions. Intuitively, the thinner shock layer formed in the chemically reacting flow and moving the second triple point into a more subsonic region may help to stablize the dual-jets pattern. The result of the calculation for this viscous equilibrium air model is shown in Fig. 10. A similar transition occurs again, and this time-accurate simulation indicated that the time required for the pattern transformation is less than 0.4 ms.

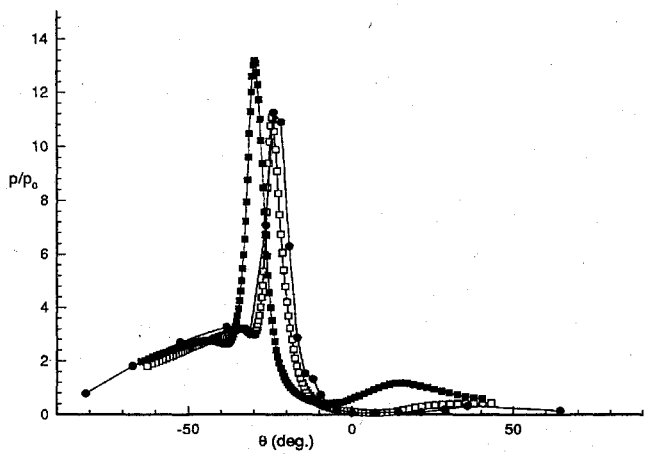

Fig. 8 Surface pressure distributions for run 83 in Ref. 12. Viscous equilibrium air model: ●, experiment; □, calculated, 1800 steps; and ■, calculated, 2700 steps.

The transition from dual type IV jets to concomitant jets might be encouraged by the existence of a strong shock stem between the two triple points. As can be seen in Fig. 1, this strong oblique shock is identified by the intersection of two pressure–deflection curves, and this intersection point is located on the upper part of one of these two curves. It is well known (see, for instance, Ref. 24) that a weak oblique shock, represented by a point located on the lower part of the pressure–deflection curve, is more likely to appear than the strong oblique shock represented by a point on the upper part of the same curve unless a strong back pressure can be supplied. In this case, the back pressure behind the stem shock does not persist, leading to the pattern change. It is observed that the flow pattern changes as the upper bow shock moves outward without an accompanying outward movement of the stem shock.

Full Tunnel Simulation

Since the initial conditions used in the traditional local simulation are by no means similar to the initial near-vacuum condition in the experimental facility, a full tunnel simulation was carried out to reconfirm the transformation of the interaction pattern.

The nozzle wall shape used in the simulations reported here was determined using a region-to-region method-of-characteristics (MOC) calculation.[24] After the nozzle contour was determined from

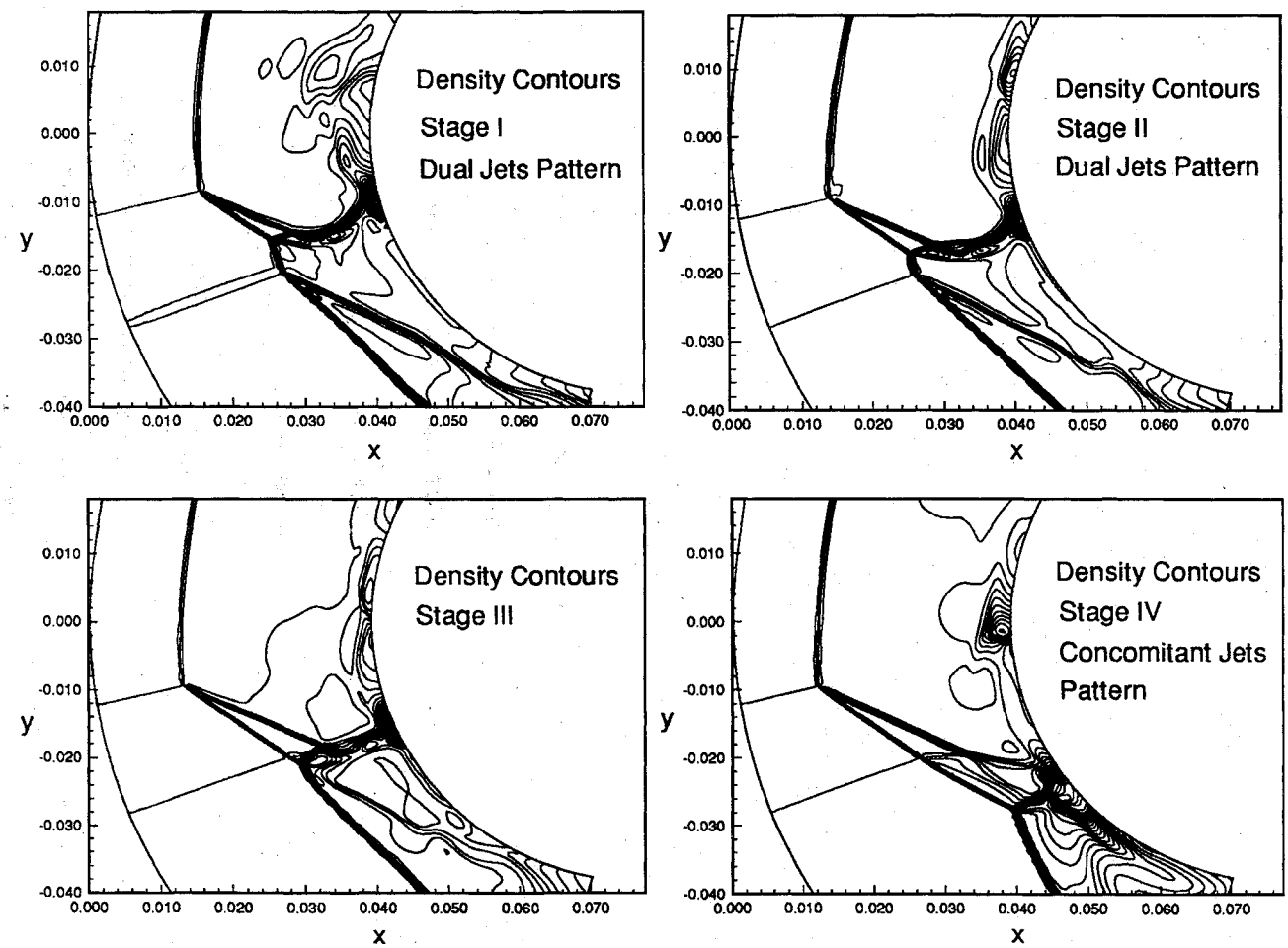

Fig. 9 Transition from the dual-jets pattern to the concomitant-jets pattern, run 86 in Ref. 12. Perfect-gas Euler solution.

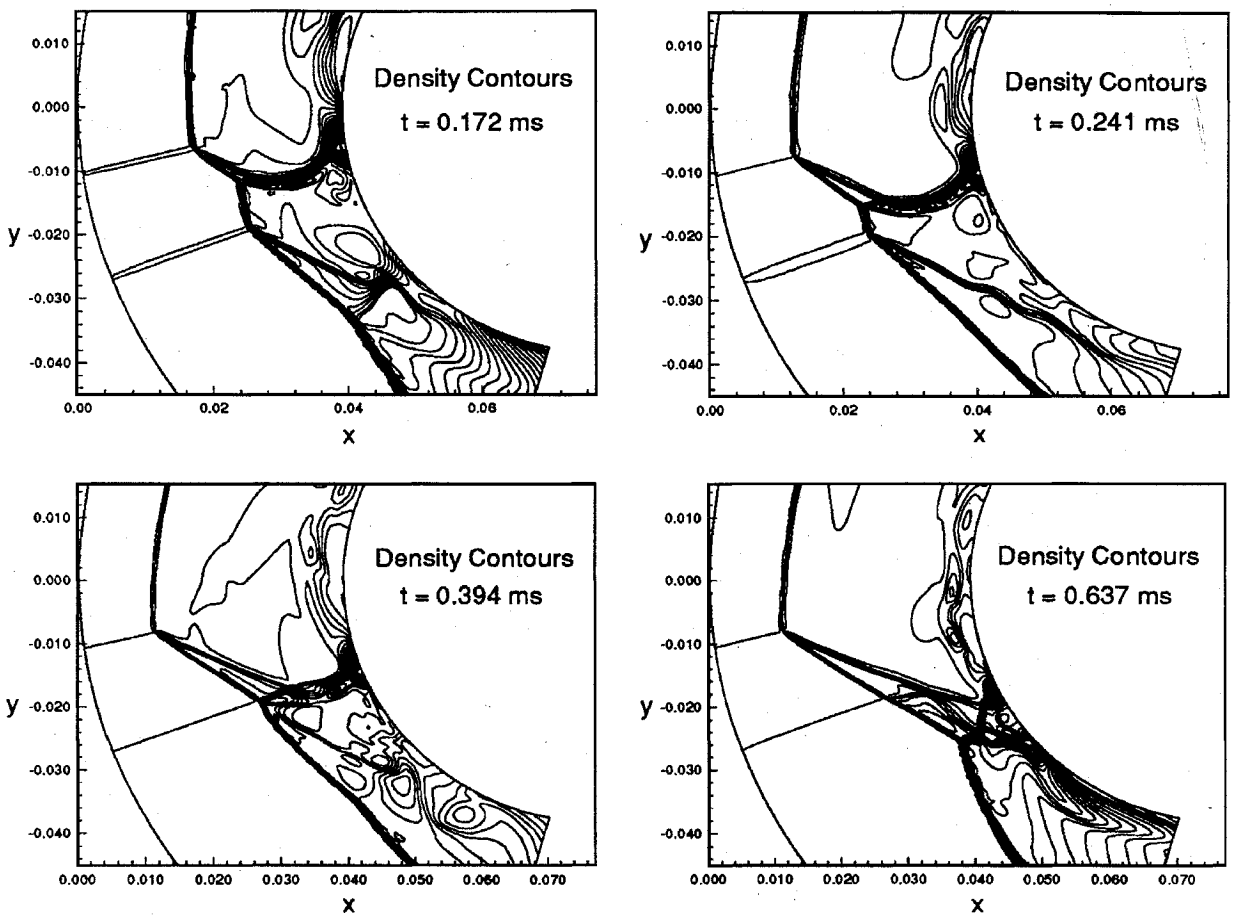

Fig. 10 Transition from the dual-jets pattern to the concomitant-jets pattern, time-accurate equilibrium viscous simulation, higher incident shock positions.

the MOC scheme, an estimated boundary-layer thickness was added to form the final shape used.

The tunnel is divided into three blocks. A 71 × 42 grid is used for the first block, a 182 × 83 grid for the second block, and a 190 × 165 grid for the third block. The tunnel is assumed to be symmetric, so only the upper half is modeled in the computational domain. A symmetry condition is applied at the centerline of the nozzle, and adiabatic no-slip boundary conditions are applied on all solid wall boundaries. A grid point coincides with the tip of the wedge. Symmetry conditions are applied in the first computational cell upstream of the tip, and wall conditions are applied in the boundary cells downstream of the tip. A local enlargement of the grid system near the model in the test section is shown in Fig. 11. Strong clustering around the incident wedge shocks is necessary; smeared oblique shocks will not give a clear interaction pattern in the relatively very small nose region of the cylinder.

Stagnation reservoir conditions are applied at the ghost cells at the nozzle inlet. These inflow boundary conditions, which are held fixed during the establishment of the flow in the hypersonic nozzle, are easy to implement and appropriate to use to model the startup process in a real impulsive-type tunnel. The inlet height must be large enough to have a small value of flow velocity at the inlet, or an anomalous wave system will be generated by the approximate Riemann solver on the grid interfaces at the nozzle inlet, resulting in a loss of total pressure. The initial pressure and temperature in the nozzle are 85 Pa and 295 K, respectively. This set of values is chosen to mimic the vacuum condition in the experiment.

Mach-number contours near the inlet early in the simulation are shown in Fig. 12. For a discussion of the evolution of the complicated wave structure that appears during the transient, the reader is referred to the paper by Tokarcik-Polsky and Cambier.[25]

The density and Mach-number distributions along the centerline of the nozzle at $t = 2.270$ ms is shown in Fig. 13. At this instant,

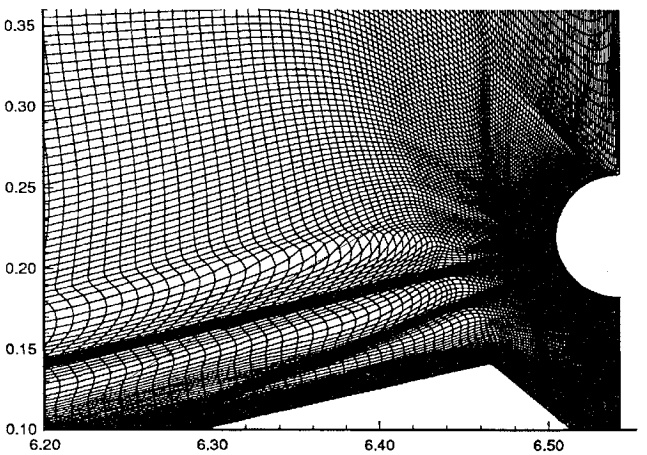

Fig. 11 Close-up view of the grid in front of the cylinder.

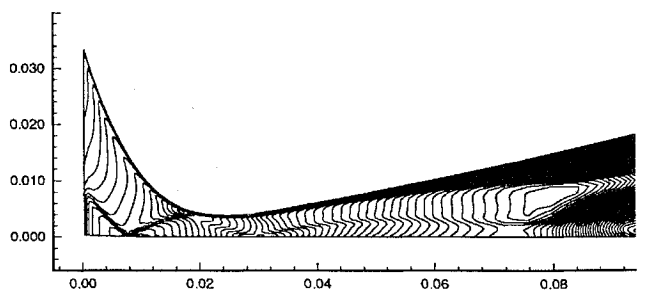

Fig. 12 Mach-number contours near the inlet at $t = 0.0265$ ms.

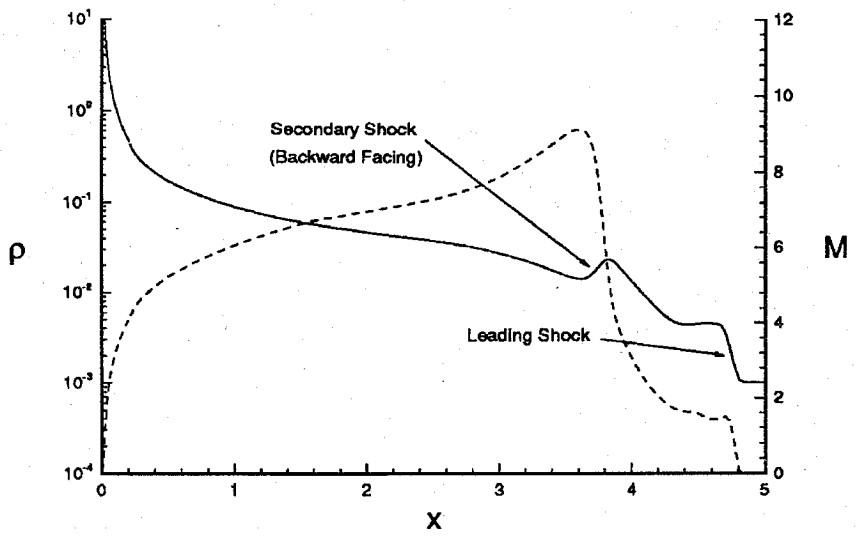

Fig. 13 Centerline density and Mach number at $t = 2.270$ ms: ——, density and - - - -, Mach number.

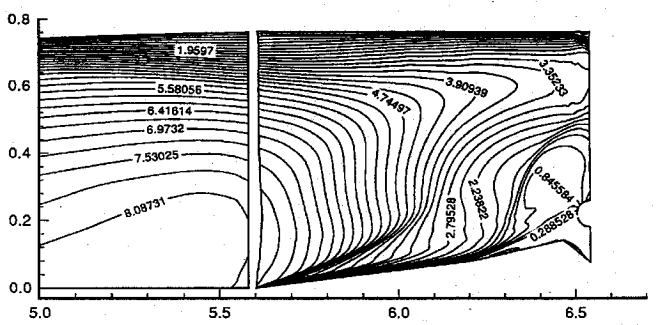

Fig. 14 Mach-number contours near the test section at $t = 4.073$ ms.

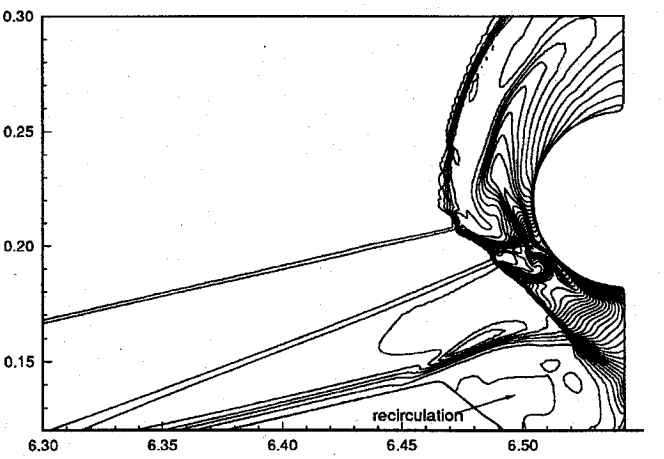

Fig. 15 Density contours at $t = 4.914$ ms, dual type IV jets, run 86 in Ref. 12.

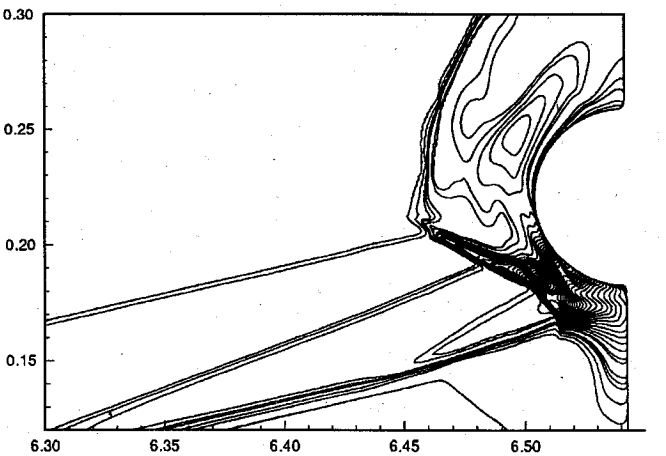

Fig. 16 Density contours at $t = 5.0$ ms, concomitant-jets, run 86 in Ref. 12.

the unsteady wave system consists of a leading shock wave followed by a weak expansion (which is barely discernable), a contact surface, a secondary shock, and finally a strong expansion wave. The secondary shock moves upstream relative to the fluid, but its net motion is down the nozzle because of the high flow velocity. The wave system observed in this numerical solution agrees with the experimental study reported in Ref. 26 as well as the result of a similar unsteady wind-tunnel simulation.[27] As described by Smith,[26] the details of the wave structure, especially the overshoot behind the leading shock, are highly dependent on the initial pressure in the nozzle. The Mach number and velocity overshoots decrease as the wave system moves downstream. This phenomenon is also observed and discussed in Ref. 27.

At time $t = 0.47$ ms, the first block reaches steady state and is removed from the calculation cycle. The second block is not taken out until $t = 4.55$ ms. Around $t = 3.2$ ms, the first wave system moves past the cylinder. As described in Ref. 27, the steady state is reached after a second wave system passes through the test section. An early stage of the passage of the second wave system is depicted in Fig. 14, which corresponds to time $t = 4.073$ ms. Because the Mach number is increasing as the second wave system passes through the test section, the incident shocks generated by the wedges are approaching the cylinder from above instead of from below.

It is interesting to note that the early bow shock grows outward (i.e., upstream) rapidly when the cylinder is located between the two wave systems. When the second wave system touches the cylinder, the Mach number of the flow around the cylinder increases dramatically, and the bow shock moves back toward the cylinder. Then, after the ramp shock reaches and interacts with the bow shock, the upper part of the bow shock starts to move out again.

As shown in Fig. 15, the dual-jets pattern appears clearly at time $t = 4.914$ ms. Unfortunately, because of the difficulties encountered in clustering the grid even more strongly around the cylinder, the resolution obtained in the full tunnel simulation is not comparable to that obtained in local simulation. Nevertheless, the transition to the concomitant-jets pattern, completed around $t = 5.1$ ms, is clearly seen in Fig. 16. The computation is stopped at this time. The transition found and discussed in the local simulations is thus confirmed.

VI. Concluding Remarks

Traditional local simulations are performed to study the properties of the shock interference problem caused by dual incident shocks. A comparison of numerical solutions with experimental

data shows the present numerical simulation is satisfactory. The position of the second impinging shock significantly changes the pattern and the peak values of pressure and heat transfer. Experimentally observed type IV interaction patterns are successfully reproduced in the present numerical simulation. For the problem we have studied here, the concomitant-jets pattern has been found to be the only possible quasi-steady-state solution. The dual-jets pattern is shown to be a transient phenomenon that eventually transforms to the concomitant-jets pattern. The unsteadiness of the pattern of dual type IV jets is closely related to the existence of a strong stem shock that connects two triple points. This stem shock becomes a weaker transmitted shock in the concomitant-jets pattern.

Using a successive multiblock technique, numerical simulation of the startup of a shock tunnel is shown to be practical, and is performed to study the time needed for the transient to die out. The available run time of the experimental facility must be longer than a predicted minimum time; otherwise the data obtained may not be an accurate representation of the quasi-steady-state solution. It has been found that the application of Edney's approximate method for identification of possible flow patterns should be performed with care, especially in cases of complicated shock–shock interference generated by multiple shock impingement, where the approximate flow pattern predicted by drawing pressure–deflection diagrams does not always correspond to the true steady or quasisteady solution.

Acknowledgments

Cray C90 computer time and user assistance provided by Cray Research is gratefully acknowledged. The authors are also grateful to Dale A. Anderson and Frank K. Lu for many useful discussions related to this work.

References

[1]Edney, B. E., "Anomalous Heat Transfer and Pressure Distributions on Blunt Bodies at Hypersonic Speeds in the Presence of an Impinging Shock," Aeronautical Research Inst. of Sweden, FFA Rept. 115, Stockholm, Sweden, Feb. 1968.

[2]Bushnell, D. M., "Interference Heating on a Swept Cylinder in Region of Intersection with a Wedge at Mach Number 8," NASA TN D-3094, 1965.

[3]Glass, C., Wieting, A. R., and Holden, M. S., "Effect of Leading Edge Sweep on Shock–Shock Interference Heating at Mach 8," AIAA Paper 89-0273, Jan. 1989.

[4]Wieting, A. R., and Holden, M. S., "Experimental Study of Shock Wave Interference Heating on a Cylindrical Leading Edge," *AIAA Journal*, Vol. 27, No. 11, 1989, pp. 1557–1565.

[5]Stewart, J. R., Thareja, R. R., and Morgan, K., "Application of Finite Element and Remeshing Technique to Shock Interference on a Cylindrical Leading Edge," AIAA Paper 88-0368, Jan. 1988.

[6]Klopfer, G. H., and Yee, H. C., "Viscous Hypersonic Shock-on-Shock Interaction on Blunt Cowl Lips," AIAA Paper 88-0233, Jan. 1988.

[7]Prabhu, R. K., Stewart, J. R., and Thareja, R. R., "Shock Interference Studies on a Circular Cylinder at Mach 16," AIAA Paper 90-0606, Jan. 1990.

[8]Lind, C. A., "A Computational Analysis of the Unsteady Phenomena Associated with a Hypersonic Type IV Shock Interaction," Ph.D. Dissertation, Univ. of Maryland, 1994; also Lind, C. A., and Lewis, M. J., "A Numerical Study of the Unsteady Processes Associated with the Type IV Shock Interaction," AIAA Paper 93-2479, June. 1993.

[9]Vemaganti, G. R., "Laminar and Turbulent Flow Computations of Type IV Shock–Shock Interference Aerothermal Loads Using Unstructured Grids," NASA CR-195008, Oct. 1994.

[10]Prabhu, R. K., "An Implementation of a Chemical and Thermal Nonequilibrium Flow Solver on Unstructured Meshes and Application to Blunt Bodies," NASA CR-194967, Aug. 1994.

[11]Holden, M. S., Wieting, A. R., Moselle, J. R., and Glass, C., "Studies of Aerothermal Loads Generated in Regions of Shock/Shock Interaction in Hypersonic Flow," AIAA Paper 88-0477, Jan. 1988.

[12]Wieting, A. R., "Multiple Shock–Shock Interference on a Cylindrical Leading Edge," *AIAA Journal*, Vol. 30, No. 8, 1992, pp. 2073–2079; also AIAA Paper 91-1800, June 1991.

[13]Van Leer, B., "Towards the Ultimate Conservative Difference Scheme. II. Monotonicity and Conservation Combined in a Second Order Scheme," *Journal of Computational Physics*, Vol. 14, March 1974, pp. 361–370.

[14]Roe, P. L., "Approximate Riemann Solvers, Parameter Vectors, and Difference Schemes," *Journal of Computational Physics*, Vol. 43, Oct. 1981, pp. 357–372.

[15]Harten, A., "High Resolution Schemes for Hyperbolic Conservation Laws," *Journal of Computational Physics*, Vol. 49, March 1983, pp. 357–393.

[16]Van Albada, G. D., Van Leer, B., and Roberts, W. W., "A Comparative Study of Computational Methods in Cosmic Gas Dynamics," *Astronomy and Astrophysics*, Vol. 108, Jan. 1982, pp. 76–84.

[17]Vinokur, M., and Liu, Y., "Equilibrium Gas Flow Computations II: An Analysis of Numerical Formulations of Conservation Laws," AIAA Paper 88-0127, Jan. 1988.

[18]Barth, T. J., "Analysis of Implicit Local Linearization Techniques for Upwind and TVD Algorithms," AIAA Paper 87-0595, Jan. 1987.

[19]Madavan, N. K., and Rai, M. M., *Computational Analysis of Rotor–Stator Interaction in Turbomachinery Using Zonal Techniques*, Vol. 125, Progress in Astronautics and Aeronautics, AIAA, New York, 1990.

[20]Hsu, K., "Numerical Investigations of Shock–Shock Interactions in Hypersonic Flow," Ph.D. Dissertation, Univ. of Texas at Arlington, TX, May 1995.

[21]Hsu, K., and Lee, S., "A Numerical Technique for Two-Dimensional Grid Generation with Grid Control at All of the Boundaries," *Journal of Computational Physics*, Vol. 96, Oct. 1991, pp. 451–469.

[22]Anderson, D. A., and Munipalli, R., private communication, Univ. of Texas at Arlington, TX, Dec. 1994.

[23]Zhong, X., "Application of Essentially Nonoscillatory Scheme to Unsteady Hypersonic Shock–Shock Interference Heating Problems," *AIAA Journal*, Vol. 32, No. 8, 1994, pp. 1606–1616.

[24]Saad, M. A., *Compressible Fluid Flow*, Prentice–Hall, Englewood Cliffs, NJ, 1985.

[25]Tokarcik-Polsky, S., and Cambier, J. L., "Numerical Study of Transient Flow Phenomena in Shock Tunnels," *AIAA Journal*, Vol. 32, No. 5, 1994, pp. 971–978.

[26]Smith, C. E., "The Starting Process in a Hypersonic Nozzle," *Journal of Fluid Mechanics*, Vol. 24, Pt. 4, 1966, pp. 625–640.

[27]Byun, Y., Lee, J. Y., Anderson, J. D., Jr., and Kothari, A. P., "Unsteady Hypersonic Viscous Flow in Impulsive Facilities," AIAA Paper 90-0421, Jan. 1990.